


Article

Influence of Co_3O_4 Nanostructure Morphology on the Catalytic Degradation of p-Nitrophenol

Huihui Chen ¹, Mei Yang ², Yuan Liu ¹, Jun Yue ^{3,*}  and Guangwen Chen ^{2,*}

¹ School of Chemistry and Chemical Engineering, Henan University of Technology, Zhengzhou 450001, China; chenhuihui@haut.edu.cn (H.C.); liuyuan2020@haut.edu.cn (Y.L.)

² Dalian Institute of Chemical Physics, Chinese Academy of Sciences, Dalian 116023, China; yangmei@dicp.ac.cn

³ Department of Chemical Engineering, Engineering and Technology Institute Groningen, University of Groningen, 9747 AG Groningen, The Netherlands

* Correspondence: yue.jun@rug.nl (J.Y.); gwchen@dicp.ac.cn (G.C.); Tel.: +31-50-363-6522 (J.Y.); +86-411-84379031 (G.C.)

Abstract: The design and fabrication of nanomaterials with controllable morphology and size is of critical importance to achieve excellent catalytic performance in heterogeneous catalysis. In this work, cobalt oxide (Co_3O_4) nanostructures with different morphologies (nanoplates, microflowers, nanorods and nanocubes) were successfully constructed in order to establish the morphology–property–performance relationship of the catalysts. The morphology and structure of the nanostructured Co_3O_4 were characterized by various techniques, and the catalytic performance of the as-prepared nanostructures was studied by monitoring the reduction of p-nitrophenol to p-aminophenol in the presence of excess NaBH_4 . The catalytic performance was found to be strongly dependent on their morphologies. The experimental results show that the pseudo-first-order reaction rate constants for Co_3O_4 nanostructures with various shapes are, respectively, 1.49 min^{-1} (nanoplates), 1.40 min^{-1} (microflowers), 0.78 min^{-1} (nanorods) and 0.23 min^{-1} (nanocubes). The Co_3O_4 nanoplates exhibited the highest catalytic activity among the four nanostructures, due to their largest specific surface area, relatively high total pore volume, best redox properties and abundance of defect sites. The established correlation between morphology, property and catalytic performance in this work will offer valuable insight into the design and application of nanostructured Co_3O_4 as a potential non-noble metal catalyst for p-nitrophenol reduction.

Keywords: cobalt oxide; morphology control; p-nitrophenol; nanostructure; catalysis



Citation: Chen, H.; Yang, M.; Liu, Y.; Yue, J.; Chen, G. Influence of Co_3O_4 Nanostructure Morphology on the Catalytic Degradation of p-Nitrophenol. *Molecules* **2023**, *28*, 7396. <https://doi.org/10.3390/molecules28217396>

Academic Editor: Raed Abu-Reziq

Received: 13 September 2023

Revised: 30 October 2023

Accepted: 31 October 2023

Published: 2 November 2023



Copyright: © 2023 by the authors. Licensee MDPI, Basel, Switzerland. This article is an open access article distributed under the terms and conditions of the Creative Commons Attribution (CC BY) license (<https://creativecommons.org/licenses/by/4.0/>).

1. Introduction

Nanomaterials have been overwhelmingly developed in the fields of electronics, optics, biology, medicine, environmental science and catalysis in recent decades, due to their unique physical, chemical and biological properties that differ from those of bulk materials [1]. Among these, transition metal oxide nanomaterials have attracted particular research interest for potential applications in catalysis because of their abundant reserves, low cost, high stability and strong redox properties. However, the catalytic activity of transition metal oxides needs to be further improved compared with the excellent performance of noble metal catalysts [2]. Various strategies have been adopted to improve the catalytic performance of transition metal oxides, such as size control [3], crystal plane or morphology modulation [4], element doping, surface defect fabrication [5], pore introduction [6] and compound recombination [7]. For example, atomically dispersed Co catalysts anchored in porous nitrogen-doped carbon ($\text{Co}_{\text{SA}}\text{-N-C}$) showed outstanding performance in removing low concentrations of HCHO at room temperature [8]. The catalytic activity of Ce-doped CuMn_8O_x (2.5% Ce; molar percentage) was found to be higher than that of CuMn_8O_x for the oxidation of CO at a lower temperature (65°C) [9]. Due to the synergistic effect of

ZIF-8 and TiO₂, the ZIF-8@TiO₂ micron composite has been used as a highly efficient photocatalyst for the degradation of tetracycline [10]. Therefore, with the rapid development of nanotechnology and the use of various regulation methods, transition metal oxides as catalysts are expected to have potential in partially substituting noble metal catalysts.

As a typical transition metal oxide, Co₃O₄ has been extensively used as a heterogeneous catalyst in many important chemical processes, such as low temperature oxidation of CO [11], CH₄ combustion [12], oxygen evolution reaction [13], decomposition of H₂O₂ [14], oxidation of ethylene [15] and reduction of p-nitrophenol (p-NP) [16]. In general, the physicochemical properties of Co₃O₄ are significantly influenced by its morphology [17]; thus, it is of great significance to develop suitable preparation methods to obtain Co₃O₄ nanomaterials with controllable morphology and size in order to upgrade the properties of Co₃O₄ and further improve its catalytic performance. To date, many Co₃O₄ nanomaterials with different shapes have been successfully fabricated. For example, Yan et al. [18] synthesized Co₃O₄ nanoflower clusters by a simple low-temperature hydrothermal method. The catalytic activity of the as-prepared Co₃O₄ nanoflower clusters for the degradation of gaseous toluene appeared to be far superior to that of Co₃O₄ blocks under the same reaction conditions. Xie et al. [19] reported the synthesis of Co₃O₄ nanorods by a precipitation–calcination method. The catalyst exhibited surprisingly high catalytic activity for CO oxidation at temperatures as low as −77 °C. Ultrathin Co₃O₄ nanosheets were also synthesized by a facile solvothermal method for the catalytic oxidation of formaldehyde at room temperature [20].

p-Nitrophenol (p-NP), which is toxic, mutagenic and non-biodegradable, is one of the most common organic pollutants in industrial and agricultural wastewater. Due to its ability to bioaccumulate and its stability, effluents containing p-NP can cause serious contamination to soil and groundwater if discharged directly into the environment without treatment [21]. In addition, its accumulation and residue in the environment may irritate eyes and skin, damage the liver, kidney and nervous system, and even cause chromosomal aberrations or blood disorders in humans [22]. Many strategies have been proposed for the degradation of p-NP, such as adsorption [23], microbial degradation [24], photocatalytic degradation [25], electrochemical methods [26] and chemical reduction [27]. Compared with other techniques, the catalytic reduction of p-NP to p-aminophenol (p-AP) by an excess NaBH₄ aqueous solution is one of the most feasible and simple methods due to its high efficiency and facile operating conditions [28]. Moreover, the only reduction product, p-AP, is not only of low toxicity, but also an important intermediate in the production of various pharmaceuticals, agrochemicals, dyes, chelating agents and photographic developers [29].

The transition metal oxides, such as Co₃O₄, CuO, Fe₂O₃ and NiO, were found to be catalytically active for the reduction of p-NP to p-AP [30,31]. In addition, several studies have shown that the shape and size of the catalyst have a significant effect on the catalytic activity for the reduction of p-NP. For example, Konar et al. [32] synthesized rod-, spherical-, star-, and flower-shaped CuO nanostructures. The star-shaped CuO showed the maximum catalytic activity for the reduction of p-NP in the presence of NaBH₄, which is correlated to their higher specific surface area, positive surface charge and the presence of a high index facet. Che et al. [33] obtained leaf-like, dumbbell-like, and flower-like CuO nanostructures via a simple oil bath route by introducing different additives. The order of catalytic activity for the reduction of p-NP to p-AP is leaf-like nanosheets > dumbbell-like architectures > flower-like nanostructures. In contrast, there are only a few reports available in the literature showing the effect of Co₃O₄ morphology on the reduction of p-NP. For example, conical Co₃O₄, stacked Co₃O₄, needled Co₃O₄ and floral Co₃O₄ have been synthesized, which show remarkably enhanced activity in the reduction of p-NP than commercial Co₃O₄ catalysts. Conical Co₃O₄ exhibits the highest catalytic activity because of the more reactive surface and more superior redox properties than other Co₃O₄ catalysts [34]. However, the morphologies of these Co₃O₄ catalysts are all microballs consisting of granules, sheets, nanoneedles or petals. The morphology, structure and physicochemical properties of different metal oxides vary greatly, and their catalytic performance can be markedly different. Therefore, it would

be essential to investigate Co_3O_4 with different morphologies in order to explore the morphology–property–performance relationships and to provide insights into the design of Co_3O_4 catalysts to optimize their catalytic performance for p-NP reduction.

In this work, $\text{Co}(\text{OH})_2$ nanoplates, CoC_2O_4 nanorods and $\text{Co}(\text{OH})_2$ microflowers as catalyst precursors were synthesized by a simple precipitation method. CoC_2O_4 nanocubes were obtained by a facile hydrothermal method. Then, Co_3O_4 nanostructures with different morphologies were successfully constructed by calcining each precursor, and the as-prepared nanostructures retained the morphologies of the precursors. The composition, size, morphology and textural properties of the obtained Co_3O_4 nanostructures were characterized by various techniques, such as XRD, TEM, SEM, BET, TPR and XPS. Furthermore, the catalytic performance of Co_3O_4 with different morphologies was studied by monitoring the reduction of p-NP to p-AP in the presence of excess NaBH_4 . Then, the effect of the morphology of Co_3O_4 nanostructures on the catalytic performance was investigated, and a strong dependence was found.

2. Results and Discussion

2.1. Characterization of Co_3O_4 Nanostructures

2.1.1. XRD

Figure 1 shows the wide-angle XRD patterns of the as-prepared Co_3O_4 with different morphologies. The data used in the XRD pattern are all original data without background subtraction. These Co_3O_4 nanostructures were obtained from different precursors (the detailed materials and methods are described in Section 3). The morphology of these nanostructures is shown in Figure 2. The XRD peaks of the four samples match the JCPDS file (01-076-1802) of the cubic phase of Co_3O_4 , indicating the complete transformation of the four precursors to Co_3O_4 via high-temperature calcination. Furthermore, the characteristic diffraction patterns of these Co_3O_4 nanostructures are identical except for their different intensities, implying that the same product was obtained but the crystallinity is different. For all the samples, the diffraction peaks at 19.03° , 31.32° , 36.90° , 38.61° , 55.75° , 59.45° and 65.34° in the XRD patterns of the Co_3O_4 nanostructures are well-matched with the (1 1 1), (2 2 0), (3 1 1), (2 2 2), (4 2 2), (5 1 1) and (4 4 0) facets of the cubic Co_3O_4 , respectively. No peaks from the other phases or impurities were observed in the patterns of the Co_3O_4 nanostructures. In addition, there was an apparent increase of counts as the 2θ angle increased in the XRD patterns, especially for the Co_3O_4 nanocubes, nanorods and microflowers. This can be mainly caused by imperfect sample preparation or the sample not being aligned well during the scanning process.

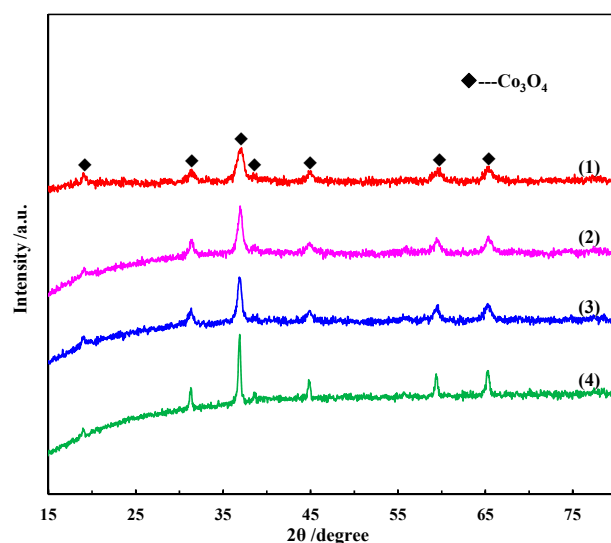


Figure 1. XRD patterns of Co_3O_4 nanostructures: (1) nanoplates, (2) microflowers, (3) nanorods and (4) nanocubes.

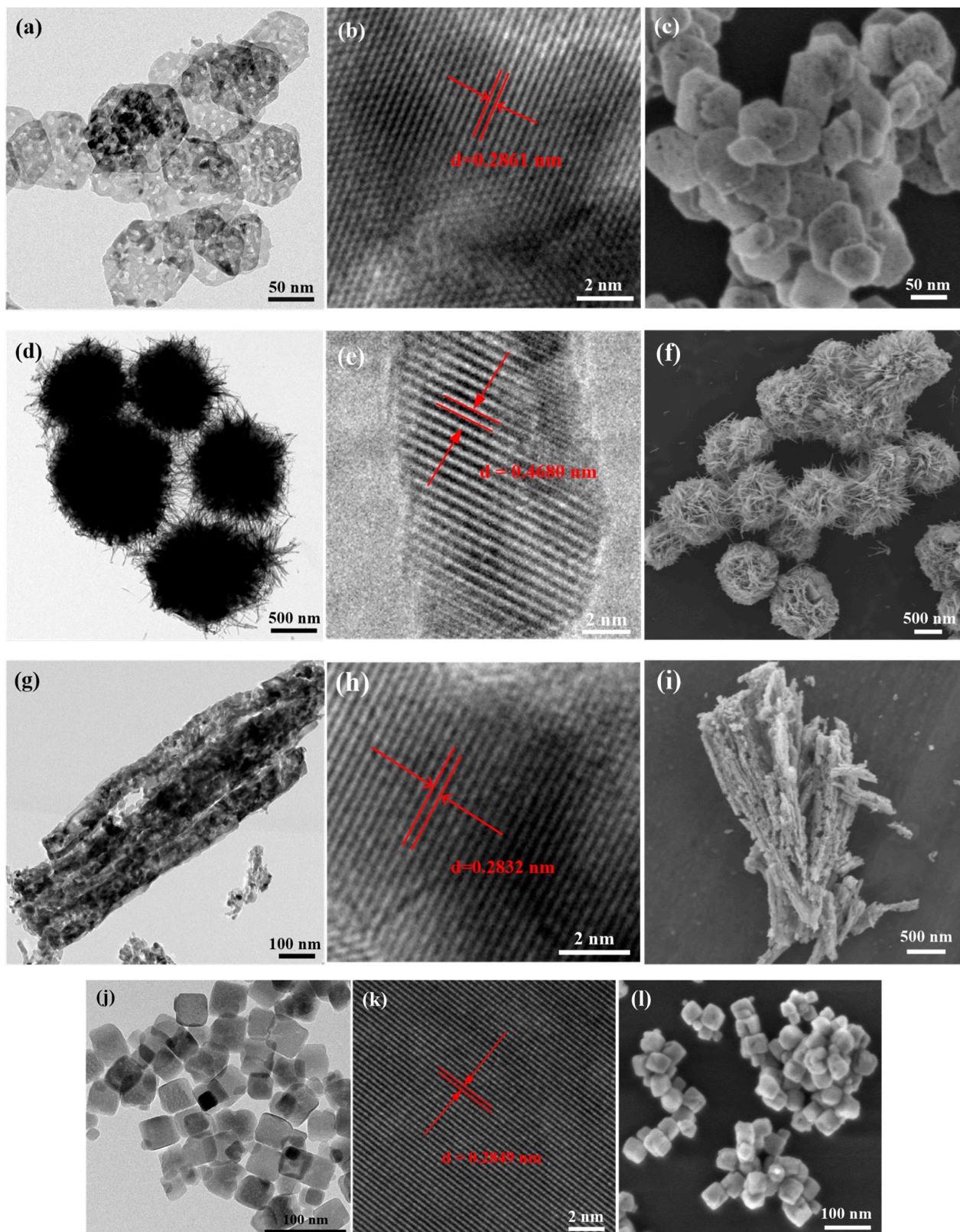


Figure 2. (a) TEM, (b) HRTEM and (c) SEM images of Co_3O_4 nanoplates; (d) TEM, (e) HRTEM and (f) SEM images of Co_3O_4 microflowers; (g) TEM, (h) HRTEM and (i) SEM images of Co_3O_4 nanorods; (j) TEM, (k) HRTEM and (l) SEM images of Co_3O_4 nanocubes.

2.1.2. TEM and SEM

The morphology and structure of the as-prepared Co_3O_4 nanostructures were investigated by scanning electron microscopy (SEM) and transmission electron microscopy (TEM) (Figure 2). As shown in Figure 2a,c, the size distribution of the as-prepared Co_3O_4 nanoplates is nearly uniform and they all consist of well-defined hexagonal plates with an average side length of about 100 nm and an average thickness of about 20 nm. Numerous mesopores with a diameter of 5–10 nm were observed on the surface of the Co_3O_4 nanoplates, which were formed by the dehydration of $\text{Co}(\text{OH})_2$ during the high-temperature calcination process. No fragment was observed in the TEM and SEM images, indicating that all the particles were assembled into hexagonal nanoplates. The Co_3O_4 microflowers, assembled by a large number of intertwined nanorods and some nanosheets, have a uniform particle size distribution, and the diameter of the Co_3O_4 microflowers ranges from 0.8 μm to 1.2 μm . Since the intersection of nanorods can form various pores, there are many interstices in the microflowers. No cracked microcrystalline flower was observed in the SEM or TEM images. In addition to the flower-like structure, some of the nanorod pieces did not form a flower-like structure (Figure 2d,f). As shown in Figure 2g,i, the Co_3O_4 nanorod samples have an average length of about 1 μm and an average width of about 100 nm. Numerous pores and gullies were clearly observed on the surface of the nanorods, which can be attributed to the release of gas from CoC_2O_4 during the high-temperature decomposition process (described in Section 3.4). It is obvious from the images that some particles have not been assembled into nanorods. As shown in Figure 2j,l, the Co_3O_4 nanocube samples all have a typical cubic shape with some very small pores on the smooth surface and an average edge length of 40 nm. Furthermore, the size distribution of the Co_3O_4 nanocubes is regular, and no fragments were observed in the images. Figure 2b,e,h,k shows the HRTEM images of these Co_3O_4 nanostructures. The lattice fringes of the Co_3O_4 nanoplates, Co_3O_4 nanorods and Co_3O_4 nanocubes with an interplanar spacing between adjacent planes of 0.28–0.29 nm are attributed to the (2 2 0) facets of the cubic Co_3O_4 (JCPDS file value, 0.29 nm). The lattice space of the Co_3O_4 microflowers is 0.4680 nm, which is comparable to the (1 1 1) plane of Co_3O_4 (JCPDS file value, 0.467 nm) and, thus, is in good accordance with the XRD result.

2.1.3. N_2 Physisorption

In general, the catalytic activity of metal oxide nanomaterials is highly dependent on their surface area and pore volume; therefore, it is indispensable to investigate the relationship between the specific surface area and porosity of these Co_3O_4 nanostructures for a better elucidation of their catalytic activity. The nitrogen adsorption–desorption isotherms and BJH adsorption pore size distributions of these Co_3O_4 nanostructures with different morphologies are plotted in Figure 3. As depicted in Figure 3a, all the as-prepared Co_3O_4 samples exhibit a type IV adsorption isotherm pattern and an H1 hysteresis loop according to the IUPAC classification, demonstrating the presence of a regular mesoporous structure [35]. The specific surface areas and pore volumes of these nanostructures based on the BET results are summarized in Table 1. The Co_3O_4 nanoplates have the largest specific surface area of $106.3 \text{ m}^2 \cdot \text{g}^{-1}$. The specific surface areas of the Co_3O_4 microflowers, nanorods and nanocubes are $69.3 \text{ m}^2 \cdot \text{g}^{-1}$, $51.2 \text{ m}^2 \cdot \text{g}^{-1}$ and $31.7 \text{ m}^2 \cdot \text{g}^{-1}$, respectively. The total pore volumes of the Co_3O_4 nanoplates and microflowers are relatively similar, being $0.27 \text{ cc} \cdot \text{g}^{-1}$ and $0.30 \text{ cc} \cdot \text{g}^{-1}$, respectively. In contrast, the Co_3O_4 nanorods and nanocubes have identical pore volumes, but the value is relatively small at only $0.21 \text{ cc} \cdot \text{g}^{-1}$. The pore size distribution derived from the adsorption branch of the Co_3O_4 nanoplates shows a broad distribution, ranging from 3.3 nm to 59.9 nm, while those of the other three Co_3O_4 samples are even broader, ranging from 1.9 nm to 78.2 nm (Figure 3b), which can be attributed to the intra-aggregated pores within the agglomerated particles [36].

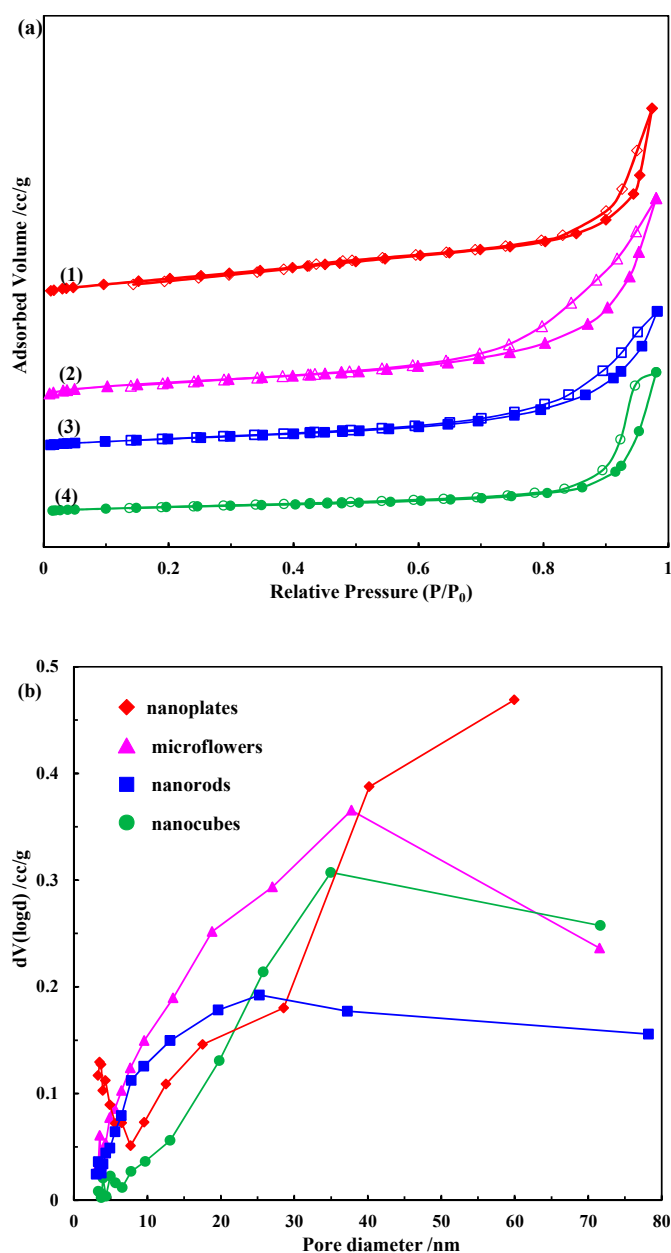


Figure 3. (a) N₂ adsorption–desorption isotherm curves of Co₃O₄ nanostructures: (1) nanoplates, (2) microflowers, (3) nanorods and (4) nanocubes; (b) BJH pore size distributions of Co₃O₄ nanostructures.

Table 1. Surface properties of Co₃O₄ nanostructures.

Catalyst	BET Surface Area (m ² /g)	Total Pore Volume (cc/g)	Average Pore Diameter (nm)
Nanoplates	106.3	0.27	3.5
Microflowers	69.3	0.30	3.5
Nanorods	51.2	0.21	7.8
Nanocubes	31.7	0.21	3.5

2.1.4. H₂-TPR

The catalytic activity of a catalyst for redox reactions depends largely on its reducibility [37]. The H₂-TPR profiles were determined to investigate the oxidation–reduction properties of the Co₃O₄ samples with different morphologies, as illustrated in Figure 4. All

four Co_3O_4 nanostructures exhibit two distinct reduction peaks in the range of 200–500 °C, corresponding to an overall two-step reduction process with CoO as the intermediate (i.e., the reduction of Co^{3+} to Co^{2+} at a relatively low temperature and then Co^{2+} to Co at a relatively high temperature), similar to that reported in the literature [38]. Curve-fitting of the TPR profiles of the Co_3O_4 nanoplates, microflowers and nanorods resulted in the resolution of three reduction sub-processes, while four reduction sub-processes were identified in the TPR curve of the Co_3O_4 nanocubes. The peak located at a relative high temperature can be deconvoluted into two adjacent peaks, indicating that the reduction of Co^{2+} to Co over all four catalysts involved the overlapping of two events, and that Co^{2+} was not completely reduced to metallic Co in one step. The peaks of the Co_3O_4 nanoplates, microflowers and nanorods at a relatively low temperature can only be deconvoluted into one peak, indicating that Co^{3+} was reduced to Co^{2+} in one step. However, the peak of the Co_3O_4 nanocubes centered around such a low temperature can be fitted with two peaks at temperatures of 287 °C and 333 °C (area ratio 1:4.2). The weak peak at 287 °C may be attributed to the reduction of a small amount of Co^{3+} to Co^{2+} [39]. The relative area of the two peaks located at the low- and high-temperature regions can be determined by means of the deconvolution above. The area ratio of the two peaks is calculated to be 1:3.44 for the Co_3O_4 nanoplates, 1:3.40 for the Co_3O_4 microflowers, 1:3.37 for the Co_3O_4 nanorods and 1:3.37 for the Co_3O_4 nanocubes, which are all close to the stoichiometric ratio of Co^{3+} to Co^{2+} in Co_3O_4 . Furthermore, all the Co_3O_4 samples were completely reduced to metallic cobalt before 500 °C. However, the peak position, peak intensity and half-peak width of these samples are different, suggesting that their redox properties are, to some extent, dependent on their morphologies. The first reduction peaks of the Co_3O_4 nanostructures are 287 °C for the Co_3O_4 nanoplates, 306 °C for the Co_3O_4 microflowers, 318 °C for the Co_3O_4 nanorods and 333 °C for the Co_3O_4 nanocubes. The results indicate that the reducibility of the Co_3O_4 nanoplates is the strongest among the four Co_3O_4 nanostructures, i.e., lattice oxygen species coordinated with Co^{3+} cations are more easily extracted from the surface of the Co_3O_4 nanoplates, thereby facilitating the electron transfer and the formation of more oxygen vacancies. This is followed by the Co_3O_4 microflowers. The decrease in reducibility of the Co_3O_4 nanorods and nanocubes can be attributed to the decrease in the specific surface areas, as observed from the BET analyses above [35].

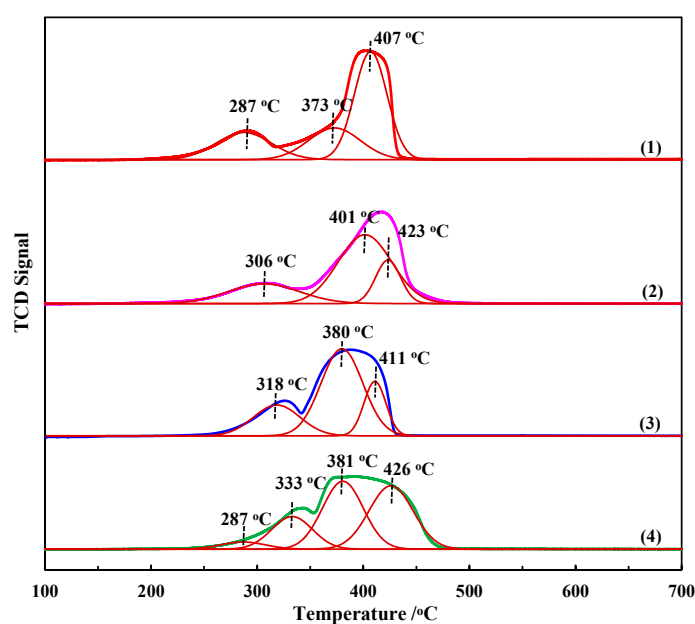


Figure 4. H_2 -TPR profiles and their deconvolution for Co_3O_4 nanostructures: (1) nanoplates, (2) microflowers, (3) nanorods and (4) nanocubes (measurement conditions: temperature from 100 °C to 700 °C at a rate of 10 °C/min using a stream of 10% H_2/Ar balance with a flow rate of 40.18 cm^3 STP/min).

2.1.5. XPS

X-ray photoelectron spectroscopy was carried out to qualitatively characterize the chemical composition and surface chemical states of these Co_3O_4 nanostructures [40]. Figure 5a shows the XPS full spectra of these nanostructures. It is evident that each peak in the spectra can be attributed to Co, O or C elements, indicating the absence of other metallic or inorganic impurities. In general, the weak C1s peak can be attributed to the hydrocarbon contaminations inherent in the XPS analysis; therefore, these Co_3O_4 nanostructures are merely constituted of Co and O elements. The high-resolution XPS spectra of the Co element of the four Co_3O_4 samples are shown in Figure 5b to provide detailed information on the chemical oxidation states. The sharp peak at the binding energy of about 779.0 eV is characteristic of Co $2p_{3/2}$ with two curve-fitted peaks corresponding to Co^{3+} (778.5~778.55 eV) and Co^{2+} (780.4~780.55 eV). The shoulder peak with a binding energy of about 794.0 eV can be deconvoluted into two typical peaks of Co^{3+} (793.6~793.7 eV) and Co^{2+} (795.5~795.7 eV), which can be attributed to the corresponding Co $2p_{1/2}$. The shake-up satellite peaks with low intensity at ca. 8.8 eV from the main spin-orbit components of Co $2p_{3/2}$ are also characteristic of Co_3O_4 . Apparently, the element Co is present in the chemical state of Co^{2+} and Co^{3+} , and there is no metallic cobalt. The molar percentages of Co^{2+} and Co^{3+} in these Co_3O_4 nanostructures are obtained according to the integrated area ratios obtained by XPS splitting, as summarized in Table 2. Our previous work has demonstrated that when Co_3O_4 is treated with a NaBH_4 aqueous solution, some of the Co^{3+} can be reduced to Co^{2+} and at the same time, oxygen vacancies are formed on the Co_3O_4 surface. More Co^{2+} on the surface of Co_3O_4 indicates that more Co^{3+} was reduced to Co^{2+} and more oxygen vacancies were formed [16]. Therefore, the amount of oxygen vacancies on the surface of the Co_3O_4 nanostructures is ordered as follows: Co_3O_4 nanoplates > Co_3O_4 nanorods > Co_3O_4 microflowers > Co_3O_4 nanocubes. Furthermore, the high-resolution O 1s spectra of these Co_3O_4 nanostructures observed at 528.9~529.2 eV can be deconvoluted into two typical peaks with binding energies of 528.9~529.2 eV and 530.0~530.4 eV, which are attributed to the lattice oxygen (O_{lat}) and the surface adsorption oxygen species (O_{sur}), respectively [41]. No characteristic peaks assigned to oxygen vacancies were observed, indicating that the amount of oxygen vacancies formed was very small.

2.2. Catalytic Performance of Co_3O_4 Nanostructures

The catalytic reduction of p-NP to p-AP in the presence of excess NaBH_4 was chosen as a probe reaction to evaluate the catalytic performance of Co_3O_4 nanostructures with different morphologies. The reaction is considered as a thermodynamically favorable process according to the standard electrode potential ($\text{p-NP/p-AP} = -0.76$ V, $\text{H}_3\text{BO}_3/\text{BH}_4^- = -1.33$ V), but it is difficult for electrons to transfer from BH_4^- to the p-NP substrate due to the large difference in the redox potential and the high kinetic barrier between the mutually exclusive negative donor (BH_4^- ions) and acceptor (p-nitrophenolate ions) [42]. Therefore, the NaBH_4 solution itself cannot reduce p-NP to p-AP in the absence of a highly efficient catalyst. Co_3O_4 has been proven as an effective catalyst for the reduction of p-NP, which can reduce the kinetic barrier [43].

Table 2. The molar percentages of Co^{2+} and Co^{3+} in Co_3O_4 nanostructures.

Catalyst	Co^{2+} (mol%)	Co^{3+} (mol%)	$\text{Co}^{3+}/\text{Co}^{2+}$
Nanoplates	34.1	65.9	1.93
Microflowers	33.8	66.2	1.96
Nanorods	33.9	66.1	1.95
Nanocubes	33.5	66.5	1.99

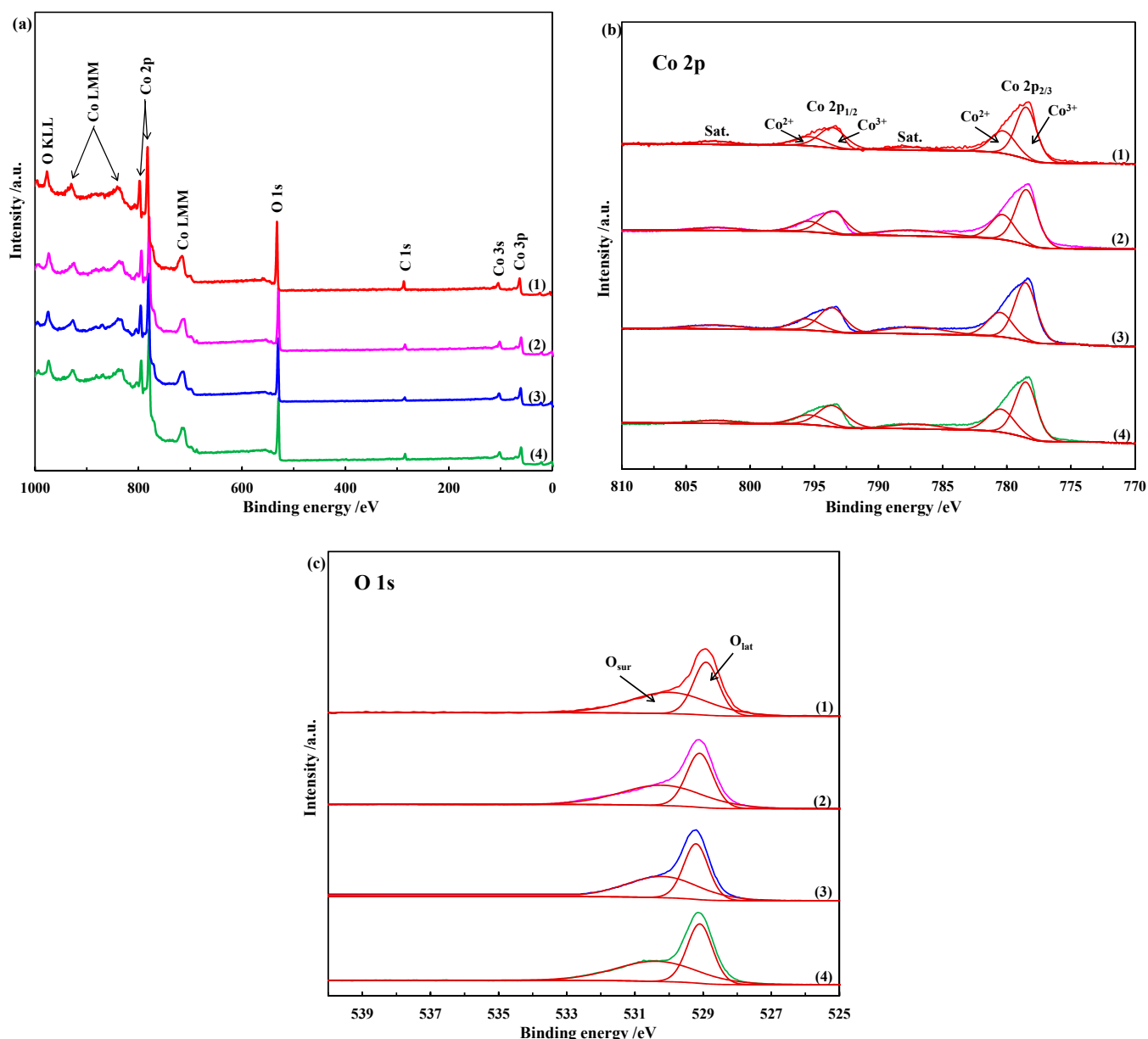


Figure 5. (a) XPS survey spectra; (b) Co 2p spectra; (c) O 1s spectra of (1) Co_3O_4 nanoplates, (2) Co_3O_4 microflowers, (3) Co_3O_4 nanorods and (4) Co_3O_4 nanocubes.

The catalytic reduction of p-NP to p-AP using Co_3O_4 nanostructures as a catalyst was conducted in a standard quartz cell and monitored by an in situ UV-vis spectrophotometer. The p-NP solution was first homogeneously mixed with a NaBH_4 solution, and then different shapes of Co_3O_4 nanostructures were added to initiate the reduction reaction. The pale-yellow aqueous solution of p-NP exhibited a strong absorption peak centered at 317 nm, as shown in Figure 6. When the NaBH_4 aqueous solution was added, the absorption peak was red-shifted to 400 nm, accompanied by a color change to green-yellow, which could be attributed to the formation of p-nitrophenolate ions (i.e., p-NP anions) under alkaline conditions [44]. When the Co_3O_4 nanostructures were introduced into the mixed solution of p-NP and NaBH_4 , the absorption peak of p-NP at 400 nm gradually decreased with the fading of the yellow color and the simultaneous appearance of a new absorption peak at 300 nm (which can be attributed to the formation of p-AP). The absorption peak at 400 nm was significantly stronger than that at 300 nm; therefore, the progress or kinetics

of the reaction was measured based on the concentration of p-NP anions in the reaction mixture by monitoring the change in the absorbance at 400 nm at different time intervals.

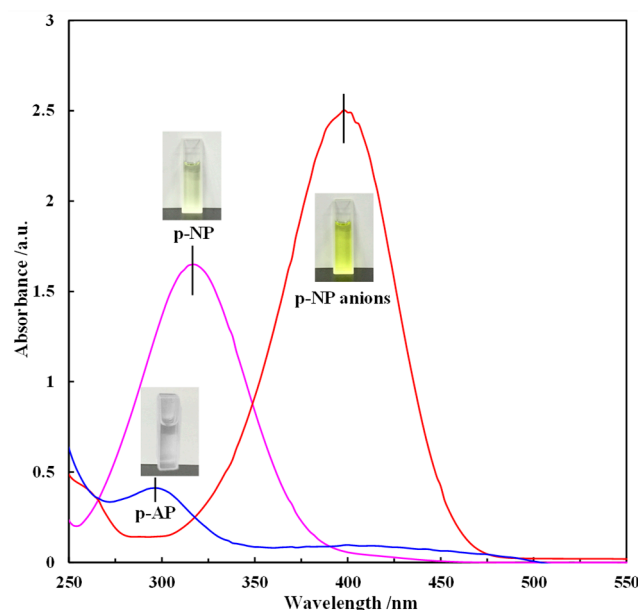


Figure 6. UV-vis absorption spectra of p-NP, p-NP anions and p-AP.

2.2.1. Catalytic Activity Test

Figure 7 shows the extinction UV-vis absorption spectra of p-NP after reaction for different durations in the presence of 0.2 mg of Co_3O_4 nanostructures with different morphologies. It can be seen that the absorption peak of p-NP at 400 nm decreased with time and a new peak was simultaneously generated at a wavelength of 300 nm, indicating the reduction of p-NP to p-AP. Figure 7a–d shows that with the prolongation of the reaction, the decrease rate of the peak intensity at 400 nm varies greatly among these Co_3O_4 nanostructures, implying that different shapes of Co_3O_4 have different catalytic activities for the p-NP reduction reaction. When the Co_3O_4 nanoplates were used as catalyst, the time to complete the reduction process was less than 3.9 min (Figure 7a). The complete conversion of p-NP to p-AP in the presence of Co_3O_4 microflowers took 5.4–6.0 min (Figure 7b). These are in comparison with 10.7 min to complete the reaction over Co_3O_4 nanorods (Figure 7c) and approximately 30.0 min over Co_3O_4 nanocubes (Figure 7d). Thus, Co_3O_4 nanoplates render the best catalytic activity, followed by Co_3O_4 microflowers, then nanorods and, finally, nanocubes.

In addition to the different time required for the complete conversion of p-NP to p-AP over these Co_3O_4 nanostructures, an induction time (t_0) is present, during which no reaction occurred initially. The induction time of these Co_3O_4 nanostructures differs significantly, as summarized in Table 3. The order of induction time required for the reduction of p-NP catalyzed by these Co_3O_4 catalysts is as follows: nanoplates < microflowers < nanorods < nanocubes, which is consistent with the order of the catalytic activity, that is, the shorter the induction time, the higher the catalytic activity. There have been many reports on the existence and happenstance of the induction time. Three main hypotheses have been found in the literature, namely, the spontaneous reconstruction time of the catalyst surface, the activation time of the catalyst active site, and the time required for reactants to diffuse onto the catalyst surface; however, the existence of the induction time is still controversial, and a concrete reason needs to be further verified [45].

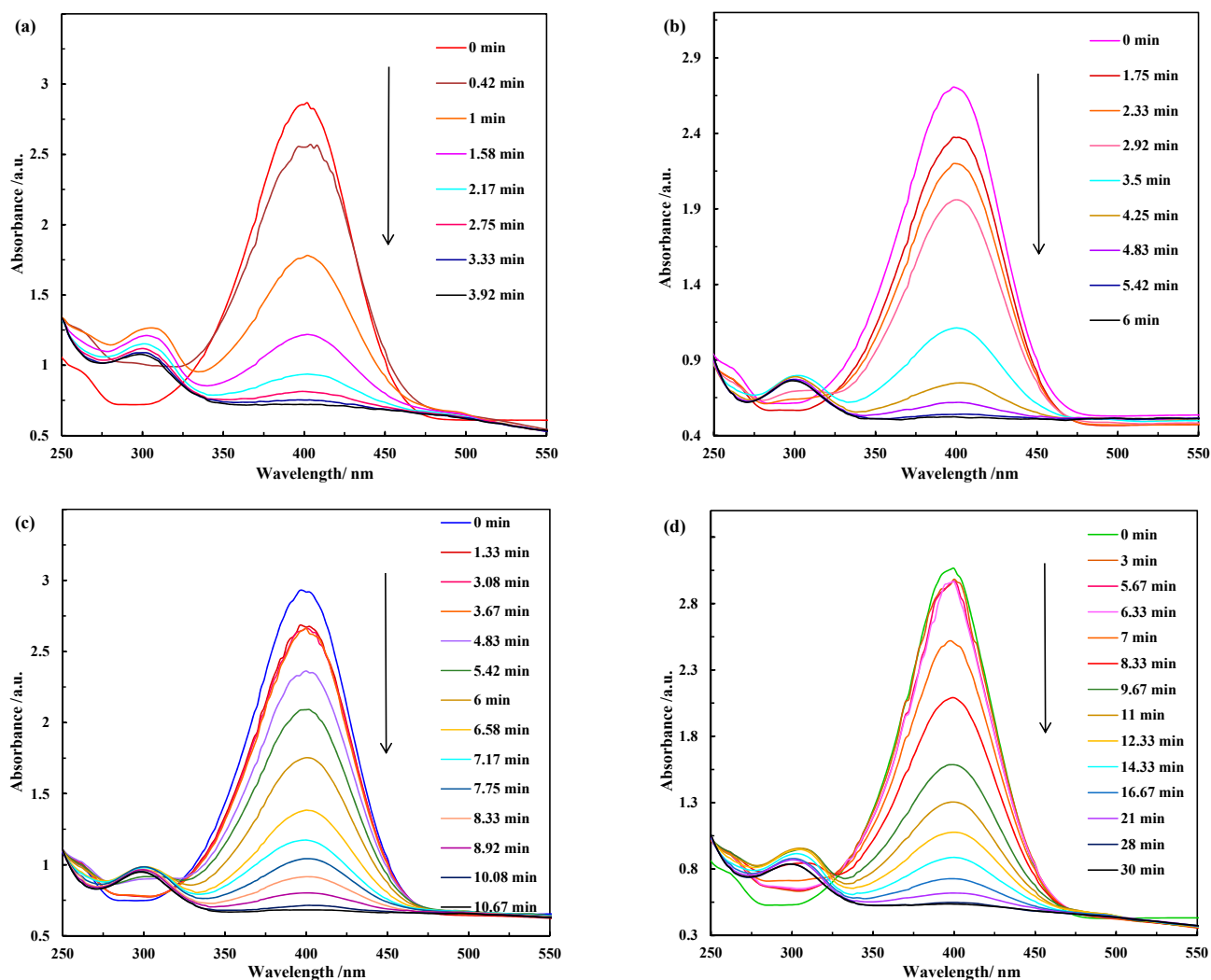


Figure 7. The evolution of UV-vis absorption spectra during the catalytic reduction of p-NP in the presence of different catalysts: (a) Co_3O_4 nanoplates, (b) Co_3O_4 microflowers, (c) Co_3O_4 nanorods, (d) Co_3O_4 nanocubes. $C_{\text{p-NP}} = 0.125$ mmol/L, $\text{NaBH}_4/\text{p-NP} = 100$, $m_{\text{cat}} = 0.2$ mg.

Table 3. The induction times of various Co_3O_4 nanostructures for the reduction of p-NP ^a.

Catalyst	t_0/min
Nanoplates	$t_0 < 0.42$
Microflowers	$t_0 < 1.75$
Nanorods	$4.25 < t_0 < 4.83$
Nanocubes	$6.33 < t_0 < 7$

^a Based on the reaction results in Figures 7 and 8.

As a typical model reaction, the kinetics of the catalytic reduction of p-NP to p-AP by NaBH_4 has been extensively investigated. In this work, the initial molar ratio of NaBH_4 to p-NP was 100, i.e., there was a significant excess of NaBH_4 . In this case, the concentration of BH_4^- remained essentially constant throughout the reaction, and the reaction rate was independent of the concentration of NaBH_4 . Then, it is reasonable to assume that the reaction follows the pseudo-first-order kinetics with respect to p-NP. The kinetic equation for the reduction reaction can be described as follows:

$$-\ln(C_t/C_0) = -\ln(A_t/A_0) = k_{\text{app}}t \quad (1)$$

where A_t and A_0 are the absorbance values of p-NP ($\lambda = 400$ nm) at time t and at the initial time, respectively. C_t and C_0 represent the equivalent concentrations of the p-nitrophenolate ions obtained from A_t and A_0 , respectively. k_{app} and t represent the apparent rate constant and reaction time, respectively. Therefore, the apparent rate constant values of these Co_3O_4 nanostructures are determined by the slopes of the respective linear curves of t versus $-\ln(A_t/A_0)$. As shown in Figure 8, the apparent rate constant values for the p-NP reduction reaction in the presence of 0.2 mg of different shapes of Co_3O_4 are 1.49 min^{-1} (nanoplates), 1.40 min^{-1} (microflowers), 0.78 min^{-1} (nanorods) and 0.23 min^{-1} (nanocubes). The activity sequence for the reduction of p-NP catalyzed by Co_3O_4 with different morphologies is as follows: Co_3O_4 nanoplates > Co_3O_4 microflowers > Co_3O_4 nanorods > Co_3O_4 nanocubes.

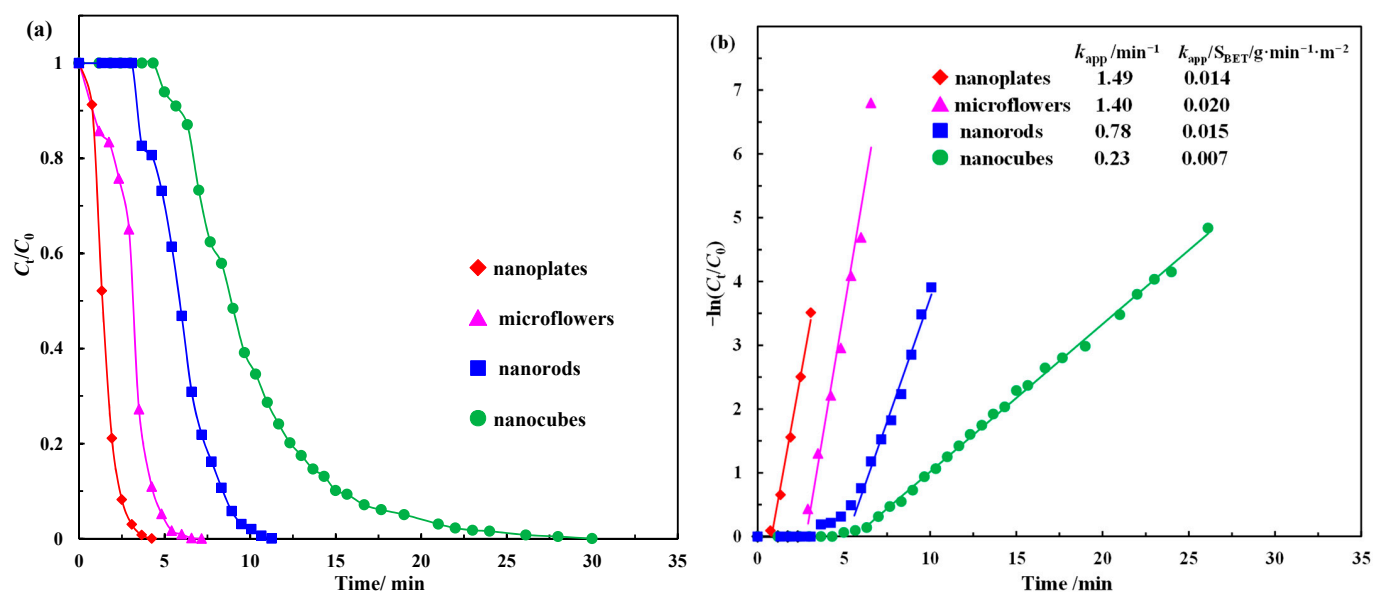


Figure 8. (a) C_t/C_0 as a function of reaction time; (b) kinetic analysis over different Co_3O_4 nanostructure catalysts reduced by aqueous NaBH_4 . $C_{p\text{-NP}} = 0.125 \text{ mmol/L}$, $p\text{-NP}/\text{NaBH}_4 = 100$ (molar ratio), $m_{cat} = 0.2 \text{ mg}$ (catalyst weight).

The literature has demonstrated that the reduction of p-NP to p-AP is a surface-controlled process that can be analyzed by the Langmuir–Hinshelwood mechanism [35]. The model reaction assumes that p-NP ions and BH_4^- are competitively adsorbed on the surface of Co_3O_4 . The adsorbed BH_4^- reacts with the Co_3O_4 surface to transfer active hydrogen species and electrons to the surface. These Co_3O_4 catalysts with different morphologies then serve as catalysts to relay active hydrogen species and electrons to the adsorbed p-NP anions to form p-AP, which is considered as the rate-determining step. The generated p-AP is then desorbed from the catalyst surface to expose the active sites for the next reduction cycle. The adsorption and desorption processes are supposed to be fast; therefore, the efficient adsorption of p-NP and BH_4^- and the efficient desorption of p-AP, as well as the superior electron transport capacity are key factors for the excellent activity of a catalyst [46]. It is well known that the surface properties of the catalyst can be tailored by controlling the morphology, size, composition and porosity of the catalyst, thereby improving its catalytic performance [47,48]. Different morphologies of Co_3O_4 are associated with different exposed crystalline planes, specific surface area, surface defects, pore structure and reducibility, which can, in turn, have a significant impact on their catalytic performance [49].

In general, the large specific surface area of the catalyst is conducive to the adsorption of reactant molecules (i.e., BH_4^- and p-NP) on its surface, and its surface can expose more active sites, which largely ensures its excellent catalytic performance. According to the BET results in Figure 3, the specific surface areas of the Co_3O_4 nanoplates, microflow-

ers, nanorods and nanocubes are 106.3, 69.3, 51.2 and 31.7 m²/g, respectively, which is consistent with the order of their catalytic activity [33]. Pore structure is also one of the most important factors affecting catalyst performance, as the abundance of interparticle mesopores and high pore volume can provide more active surface sites for a heterogeneous catalytic reaction. It can be clearly seen from the TEM and SEM results (Figure 2) that there are many small pores on the surface of the Co₃O₄ nanoplates, and the surface of the Co₃O₄ microflowers is rough. The BET results (Figure 3 and Table 1) show that the total pore volumes of the Co₃O₄ nanoplates and microflowers are 0.27 and 0.30 cc/g, respectively, which is significantly higher than those of the Co₃O₄ nanorods and nanocubes. Despite the rough surface of the Co₃O₄ nanorods, the total pore volume is only 0.21 cc/g, which is the same as that of the Co₃O₄ nanocubes with a smooth surface. As a result, the catalytic activity of the Co₃O₄ nanoplates and microflowers is much higher than that of the Co₃O₄ nanorods and nanocubes [50]. Oxygen vacancies, as a common inherent surface defect in metal oxides, have been proven to significantly affect or even modify the physical and chemical properties of materials and are an effective means to regulate the structure and catalytic performance of catalysts. In addition, our previous results have demonstrated that oxygen vacancies can act as active sites for the reduction of p-NP [16]. The XPS results show that the amount of oxygen vacancies on the surface of Co₃O₄ nanostructures is ordered as follows: Co₃O₄ nanoplates > Co₃O₄ nanorods > Co₃O₄ microflowers > Co₃O₄ nanocubes. Therefore, the catalytic activity of the Co₃O₄ nanoplates is the highest, and that of the Co₃O₄ nanocubes is the lowest. For the reduction of p-NP, Co₃O₄ served as a catalyst to transfer active hydrogen species and electrons from the donor BH₄⁻ to the acceptor p-NP. Therefore, the reducibility of Co₃O₄ also greatly affects its catalytic performance. According to the TPR results (Figure 4), the order of the reducibility of these different Co₃O₄ catalysts is as follows: Co₃O₄ nanoplates > Co₃O₄ microflowers > Co₃O₄ nanorods > Co₃O₄ nanocubes, which is consistent with the order of their catalytic activity. In summary, different morphologies of Co₃O₄ render different properties, such as different specific surface area, surface defects, porosity and reducibility, which, in turn, significantly affect their catalytic performance.

Among these factors, the specific surface area (S_{BET}) seems to have the greatest influence on the catalytic performance, given that it is much higher for the Co₃O₄ nanoplates than that for the other shapes (Table 1). To better elucidate the role of other factors, the reaction rate constants per unit specific surface area ($k_{\text{app}}/S_{\text{BET}}$) were adopted to compare the activity of Co₃O₄ with different morphologies. The values of $k_{\text{app}}/S_{\text{BET}}$ are 0.020 g·min⁻¹·m⁻² for the Co₃O₄ microflowers, 0.015 g·min⁻¹·m⁻² for the Co₃O₄ nanorods, 0.014 g·min⁻¹·m⁻² for the Co₃O₄ nanoplates and 0.007 g·min⁻¹·m⁻² for the Co₃O₄ nanocubes (Figure 8b, Table 4). The sequence of the catalytic activity per unit-specific surface area of these Co₃O₄ nanostructures is as follows: Co₃O₄ microflowers > Co₃O₄ nanorods > Co₃O₄ nanoplates > Co₃O₄ nanocubes. The Co₃O₄ microflowers exhibited the best catalytic activity per unit specific surface area, which can be attributed to its largest total pore volume. Therefore, compared with the specific surface area and total pore volume, the effect of reducibility and surface defects is believed to be relatively small in determining the current catalyst performance.

Table 4. Comparison of the rate constants of different catalysts for the catalytic reduction of p-NP to p-AP by NaBH₄ in the recent literature and this work.

Catalyst	$m_{\text{cat}}^{\text{a}}$ g/L	k_{app} min ⁻¹	$k_{\text{nor}}^{\text{b}}$ L·min ⁻¹ ·g ⁻¹	S_{BET} m ² /g	$k_{\text{app}}/S_{\text{BET}}$ g·min ⁻¹ ·m ⁻²	Reference
Au	0.0034	0.1540	44.814	-	-	[51]
Pd	0.0462	0.7300	15.801	-	-	[52]
Hg/Pd	1.4286	3.5040	2.453	-	-	[53]
Au-Cu _x O _y in HPSNs	0.2500	0.9600	3.840	86.7	0.0111	[54]

Table 4. Cont.

Catalyst	$m_{\text{cat}}^{\text{a}}$	k_{app}	$k_{\text{nor}}^{\text{b}}$	S_{BET}	$k_{\text{app}}/S_{\text{BET}}$	Reference
	g/L	min^{-1}	$\text{L}\cdot\text{min}^{-1}\cdot\text{g}^{-1}$	m^2/g	$\text{g}\cdot\text{min}^{-1}\cdot\text{m}^{-2}$	
Au/TNT	0.3750	0.0610	0.163	124.0	0.0005	[55]
PdCu-LDHs	0.3107	1.1000	3.540	-	-	[56]
Ag-CeO ₂	0.1200	0.6560	5.467	5.6	0.1171	[57]
Co/Eatp@C	0.0500	0.6900	13.80	236.5	0.0029	[58]
PdO-Co ₃ O ₄	0.8333	1.3100	1.572	67.3	0.0195	[59]
Co ₃ O ₄ @C	1.6667	0.7550	0.453	5.1	0.1480	[60]
NiCo ₂ O ₄	0.5000	0.1260	0.252	68.4	0.0018	[61]
Co ₃ O ₄ nanoplates	0.0714	1.4900	20.868	106.3	0.0140	This work
Co ₃ O ₄ microflowers	0.0714	1.4000	19.600	69.3	0.0202	This work
Co ₃ O ₄ nanorods	0.0714	0.7800	10.920	51.2	0.0152	This work
Co ₃ O ₄ nanocubes	0.0714	0.2300	3.221	31.7	0.0073	This work

^a The mass concentration of the catalyst in the solution. ^b The mass-normalized rate constant calculated based on the catalyst amount, including the support based on the equation: $k_{\text{nor}} = k_{\text{app}}/m_{\text{cat}}$.

2.2.2. Stability Test

Considering the economic benefits and environmental factors in the practical applications, recyclability is another criterion to evaluate the performance of catalysts in addition to their catalytic activity. The recyclability of these Co₃O₄ nanostructures was evaluated by continuously adding a concentrated p-NP aqueous solution after each cycle to adjust the concentration of p-NP to its initial value of 0.125 mmol/L before the reaction. The NaBH₄ concentration in the first cycle was 12.5 mmol/L, which is 100 times the concentration of p-NP, and no NaBH₄ was added in the subsequent cycles. As can be seen from Figure 9, although the apparent rate constants of all the Co₃O₄ nanostructures are somewhat reduced, they show no significant deactivation and still maintain satisfactory stability over multiple consecutive cycles. After five consecutive cycles, the apparent rate constants could still reach 1.37 min⁻¹ for the Co₃O₄ nanoplates, 1.16 min⁻¹ for the Co₃O₄ microflowers, 0.61 min⁻¹ for the Co₃O₄ nanorods and 0.16 min⁻¹ for the Co₃O₄ nanocubes. To better evaluate the performance of the current catalysts, the activity of some common (supported) noble metal catalysts and other cobalt-based catalysts are summarized in Table 4. As can be seen from the table, the catalytic activity (k_{nor}) of the as-prepared Co₃O₄ nanoplates and Co₃O₄ microflowers in this work is comparable or even better than that of some noble metal catalysts and supported ones (e.g., Au, Pd, Au-Cu_xO_y in HPSNs and Ag-CeO₂) and is significantly higher than that of other cobalt-based catalysts (e.g., PdO-Co₃O₄, NiCo₂O₄, and Co₃O₄@C). The results here clearly demonstrate the relatively high efficiency of the Co₃O₄ nanoplates and microflowers for the catalytic reduction of p-NP.

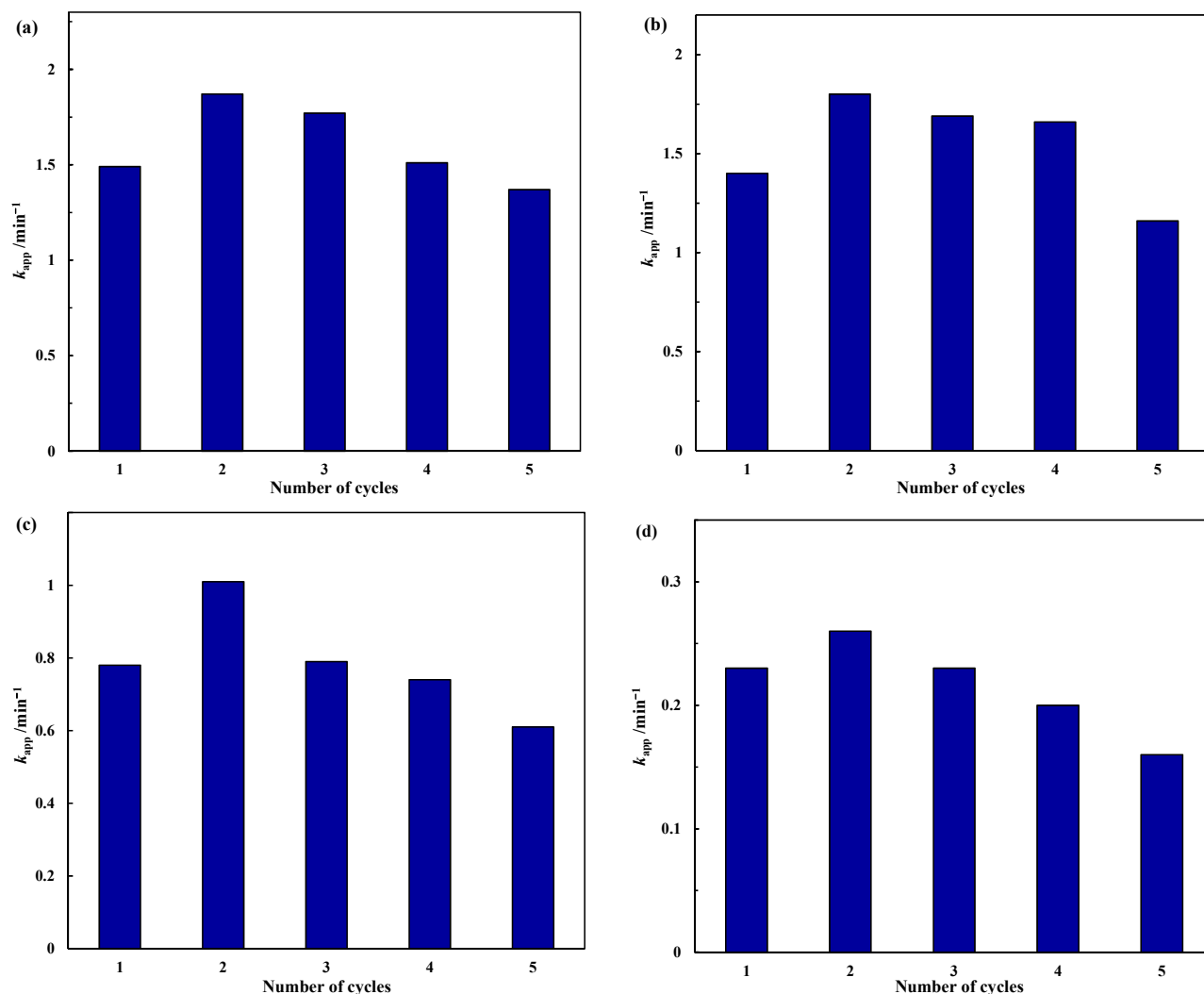


Figure 9. Recyclability of Co_3O_4 nanostructures for the catalytic reduction of p-NP to p-AP by excess NaBH_4 : (a) Co_3O_4 nanoplates; (b) Co_3O_4 microflowlers; (c) Co_3O_4 nanorods; (d) Co_3O_4 nanocubes. $C_{\text{p-NP}} = 0.125$ mmol/L, p-NP/ $\text{NaBH}_4 = 100$, $m_{\text{cat}} = 0.2$ mg.

3. Materials and Methods

3.1. Materials

Cobalt nitrate hexahydrate ($\text{Co}(\text{NO}_3)_2 \cdot 6\text{H}_2\text{O}$), cobalt acetate tetrahydrate ($\text{Co}(\text{CH}_3\text{COO})_2 \cdot 4\text{H}_2\text{O}$), cobalt chloride hexahydrate ($\text{CoCl}_2 \cdot 6\text{H}_2\text{O}$), sodium hydroxide (NaOH), urea ($\text{CO}(\text{NH}_2)_2$), oxalic acid ($\text{H}_2\text{C}_2\text{O}_4$), polyvinyl pyrrolidone K90 ($(\text{C}_6\text{H}_9\text{NO})_n$, PVP), sodium dodecyl benzene sulfonate ($\text{C}_{18}\text{H}_{29}\text{NaO}_3\text{S}$, SDBS), sodium borohydride (NaBH_4) and p-nitrophenol ($\text{C}_6\text{H}_5\text{NO}_3$) of analytical grade were purchased from Aladdin Industrial Corporation (Shanghai, China). All the chemicals were used as received without further treatment. Deionized water was used in all the experiments.

3.2. Preparation of $\text{Co}(\text{OH})_2$ Nanoplates

The $\text{Co}(\text{OH})_2$ nanoplates were synthesized according to our previous work [16]. Briefly, $\text{CoCl}_2 \cdot 6\text{H}_2\text{O}$ (5 mmol) and NaOH (50 mmol) were dissolved separately in 50 mL deionized water. The precipitation was started by the dropwise addition of CoCl_2 and NaOH aqueous solutions into a three-necked flask containing 50 mL deionized water at 50°C under N_2 atmosphere. The obtained pink suspension was stirred at 50°C for 1 h. The N_2 flow was then stopped. The product was cooled to room temperature, centrifuged, washed several times with deionized water and dried in the oven (60°C) for 8 h.

3.3. Preparation of $\text{Co}(\text{OH})_2$ Microflowers

The $\text{Co}(\text{OH})_2$ microflowers were synthesized by a simple precipitation method. In a typical experiment, $\text{Co}(\text{NO}_3)_2 \cdot 6\text{H}_2\text{O}$ (4 mmol) and $\text{CO}(\text{NH}_2)_2$ (0.5 mol) were dissolved in 50 mL deionized water. Then, polyvinyl pyrrolidone (3.85 μmol) was added to the solution described above. The mixture was ultrasonicated for 1 h to form a homogeneous solution. The solution was then transferred to a three-necked flask and heated in a water bath at 80 °C for 6 h with magnetic stirring. The flask was semi-sealed during the reaction process. Finally, a purple precipitate was obtained. After cooling to room temperature, the purple precipitate was centrifuged, washed several times with deionized water and dried in the oven (60 °C) for 8 h.

3.4. Preparation of CoC_2O_4 Nanorods

The CoC_2O_4 nanorods were synthesized by a simple precipitation method. Briefly, $\text{Co}(\text{CH}_3\text{COO})_2 \cdot 4\text{H}_2\text{O}$ (5.9 mmol) and NaOH (10 mmol) were dissolved into 50 mL and 10 mL deionized water, respectively. Then, 0.6 g of $\text{H}_2\text{C}_2\text{O}_4$ was added to the $\text{Co}(\text{CH}_3\text{COO})_2$ aqueous solution. The precipitation process was started by the dropwise addition of a NaOH aqueous solution into the $\text{Co}(\text{CH}_3\text{COO})_2$ aqueous solution under continuous stirring. The obtained pink suspension was stirred at 85 °C for 12 min. The product was cooled to room temperature, centrifuged, washed several times with deionized water and dried in the oven (60 °C) for 8 h.

3.5. Preparation of CoC_2O_4 Nanocubes

The CoC_2O_4 nanocubes were synthesized by a facile hydrothermal method. In a typical synthesis, 4 mmol $\text{Co}(\text{CH}_3\text{COO})_2 \cdot 4\text{H}_2\text{O}$ and 5 mmol NaOH were dissolved in 20 mL deionized water, respectively. The precipitation was initiated at room temperature by the dropwise addition of a NaOH aqueous solution to the $\text{Co}(\text{CH}_3\text{COO})_2$ aqueous solution with continuous stirring. The obtained suspension was stirred for another 0.5 h at room temperature. Then, 1.2 g SDBS was added to the suspension described above. The suspension was transferred to a 100 mL Teflon-lined stainless-steel autoclave, and then the autoclave was maintained at 160 °C for 36 h. The temperature was programmed to increase from room temperature to 160 °C at a heating rate of 2.0 °C/min. After cooling to room temperature, the black precipitate was centrifuged, washed several times with deionized water and dried in the oven (60 °C) for 8 h.

3.6. Preparation of Reduced Co_3O_4

The as-prepared $\text{Co}(\text{OH})_2$ nanoplates, $\text{Co}(\text{OH})_2$ microflowers, CoC_2O_4 nanorods and CoC_2O_4 nanocubes were calcined at 300 °C for 2 h in air to obtain the corresponding Co_3O_4 nanostructures. The temperature was programmed to increase from room temperature to 300 °C at a ramp of 2 °C/min. Then, these Co_3O_4 nanostructures were separately soaked in a NaBH_4 aqueous solution (0.05 mol/L) at 30 °C for 40 min. Afterwards, the powder was collected via centrifugation, washed several times with deionized water and used directly for the catalytic reduction of p-NP to p-AP.

3.7. Catalyst Characterization

The powder X-ray diffraction (XRD) analyses of the as-prepared samples at room temperature were recorded by a PANalytical X'pert-Pro powder X-ray diffractometer equipped with Cu Ka monochromatic radiation ($\lambda = 0.1541$ nm) with 2θ ranging from 10° to 90° at a scanning rate of 5°/min. The X-ray tube was operated under 40 kV and 40 mA. Nitrogen sorption measurements of the samples were performed on a Quadrasorb SI adsorption analyzer. The specific surface areas and pore properties were calculated from the adsorption–desorption isotherms collected at 77 K. Transmission electron microscopy (TEM) were taken on a JEOL JEM-2100 at an accelerating voltage of 120 kV, and scanning electron microscopy (SEM) were taken on a JEOL JSM-7800F at an accelerating voltage of 3 kV to examine the morphologies of the as-prepared samples. Temperature-programmed

reduction (H_2 -TPR) was carried out on a Micromeritics AutoChem 2920 apparatus. A 10% mixture of H_2 /Ar passed through the catalyst bed at a flow rate of 40 mL min^{-1} , and at the same time, the temperature was programmed to increase from $50 \text{ }^\circ\text{C}$ to $700 \text{ }^\circ\text{C}$ at a heating rate of $10 \text{ }^\circ\text{C/min}$.

3.8. Catalytic Reduction of p-NP to p-AP by Excess $NaBH_4$

The catalytic reduction of p-NP to p-AP was conducted under controllable conditions to evaluate the catalytic performance of the obtained nanostructures. Typically, the reduction reaction was conducted in a 3.5 mL standard quartz cell at room temperature (ca. $23 \text{ }^\circ\text{C}$). Excess $NaBH_4$ aqueous solution was chosen as the reducing agent. Approximately 2.0 mL p-NP aqueous solution (0.175 mmol/L) was first mixed with 0.7 mL freshly prepared $NaBH_4$ solution (0.05 mol/L) in the quartz cell. Then, 0.1 mL suspension containing one of the obtained Co_3O_4 nanostructures (2 g/L) was quickly injected into the mixture under temperature control and rapid stirring. The reduction process was monitored by detecting the extinction of p-NP via an in situ UV-vis spectrophotometer (METASH UV8000) over a scanning range of 200 nm–600 nm. The kinetic evaluation was judged by the disappearance of the p-NP adsorption peak at 400 nm as a function of the reaction time.

4. Conclusions

Co_3O_4 nanoplates, microflowers, nanorods and nanocubes were successfully synthesized by facile precipitation or hydrothermal methods, followed by a thermal decomposition process. The catalytic performance of these Co_3O_4 nanostructures for the reduction of p-NP to p-AP in the presence of excess $NaBH_4$ was studied. The order of the catalytic activity of these Co_3O_4 nanostructures is nanoplates > microflowers > nanorods > nanocubes. Co_3O_4 nanoplates exhibit the highest catalytic activity due to their largest specific surface area, relatively high total pore volume, abundant oxygen vacancies and strong reducibility. The results indicate that Co_3O_4 catalysts with different morphologies exhibit different properties, such as different specific surface area, porosity, surface defects and reducibility, which, in turn, significantly affect their catalytic performance. Therefore, morphology control in the preparation of Co_3O_4 nanocrystals is crucial for the preparation of highly efficient heterogeneous catalysts. The controllable synthesis of Co_3O_4 nanostructures with different morphologies is expected to bring new opportunities for regulating the catalytic performance of metal oxide catalysts.

Author Contributions: Conceptualization, H.C. and M.Y.; methodology, H.C. and M.Y.; formal analysis, H.C. and J.Y.; investigation, H.C. and Y.L.; writing—original draft preparation, H.C.; writing—review and editing, H.C., J.Y. and G.C.; funding acquisition, G.C. and H.C. All authors have read and agreed to the published version of the manuscript.

Funding: This research was funded by the Ph.D. Foundation of Henan University of Technology (No. 2018BS047), the Innovative Funds Plan of Henan University of Technology (No.2020ZKCJ04), and the Science and Technology Foundation of Henan Province (No. 222102240066).

Institutional Review Board Statement: Not applicable.

Informed Consent Statement: Not applicable.

Data Availability Statement: All the data are available in the manuscript.

Conflicts of Interest: The authors declare no conflict of interest.

References

1. Sengul, A.B.; Asmatulu, E. Toxicity of metal and metal oxide nanoparticles: A review. *Environ. Chem. Lett.* **2020**, *18*, 1659–1683. [[CrossRef](#)]
2. Ludwig, J.R.; Schindler, C.S. Catalyst: Sustainable catalysis. *Chem* **2017**, *2*, 313–316. [[CrossRef](#)]
3. Tsunoyama, H.; Ito, H.; Komori, M.; Kobayashi, R.; Shibuta, M.; Eguchi, T.; Nakajima, A. Liquid-phase catalysis by single-size palladium nanoclusters supported on strontium titanate: Size-specific catalysts for Suzuki-Miyaura coupling. *Catal. Sci. Technol.* **2018**, *8*, 5827–5834. [[CrossRef](#)]

4. Gao, Q.X.; Wang, X.F.; Di, J.L.; Wu, X.C.; Tao, Y.R. Enhanced catalytic activity of α -Fe₂O₃ nanorods enclosed with {110} and {001} planes for methane combustion and CO oxidation. *Catal. Sci. Technol.* **2011**, *1*, 574–577. [[CrossRef](#)]
5. Peng, K.; Hou, Y.; Zhang, Y.; Liu, X.; Li, Y.; Li, B.; Zeng, Z.; Huang, Z. Engineering oxygen vacancies in metal-doped MnO₂ nanospheres for boosting the low-temperature toluene oxidation. *Fuel* **2022**, *314*, 123965. [[CrossRef](#)]
6. Zhou, W.; Fu, H. Mesoporous TiO₂: Preparation, doping, and as a composite for photocatalysis. *ChemCatChem* **2013**, *5*, 885–894. [[CrossRef](#)]
7. Chen, H.; Yang, M.; Yue, J.; Chen, G. Facile Synthesis of CoOOH nanorings over reduced graphene oxide and their application in the reduction of p-nitrophenol. *Materials* **2022**, *15*, 8862. [[CrossRef](#)]
8. Tang, H.; Zhang, J.; Huang, M.; Zhang, J.; Zhou, Y.; Wang, G.; Wang, R.; Chen, J. Remarkable performance of atomically dispersed cobalt catalyst for catalytic removal of indoor formaldehyde. *J. Colloid Interface Sci.* **2022**, *624*, 527–536. [[CrossRef](#)]
9. Dey, S.; Dhal, G.C. Ceria doped CuMnO_x as carbon monoxide oxidation catalysts: Synthesis and their characterization. *Surf. Interfaces* **2020**, *18*, 100456. [[CrossRef](#)]
10. Li, R.; Li, W.; Jin, C.; He, Q.; Wang, Y. Fabrication of ZIF-8@TiO₂ micron composite via hydrothermal method with enhanced absorption and photocatalytic activities in tetracycline degradation. *J. Alloys Compd.* **2020**, *825*, 154008. [[CrossRef](#)]
11. Lou, Y.; Wang, L.; Zhao, Z.; Zhang, Y.; Zhang, Z.; Lu, G.; Guo, Y.; Guo, Y. Low-temperature CO oxidation over Co₃O₄-based catalysts: Significant promoting effect of Bi₂O₃ on Co₃O₄ catalyst. *Appl. Catal. B-Environ.* **2014**, *146*, 43–49. [[CrossRef](#)]
12. Dou, J.; Tang, Y.; Nie, L.; Andolina, C.M.; Zhang, X.; House, S.; Li, Y.; Yang, J.; Tao, F. Complete oxidation of methane on Co₃O₄/CeO₂ nanocomposite: A synergistic effect. *Catal. Today* **2017**, *311*, 48–55. [[CrossRef](#)]
13. Xu, L.; Jiang, Q.; Xiao, Z.; Li, X.; Huo, J. Plasma-engraved Co₃O₄ nanosheets with oxygen vacancies and high surface area for the oxygen evolution reaction. *Angew. Chem. Int. Edit.* **2016**, *55*, 5277–5281. [[CrossRef](#)] [[PubMed](#)]
14. Chen, H.; Yang, M.; Tao, S.; Chen, G. Template-free synthesis of Co₃O₄ nanorings and their catalytic application. *CrystEngComm* **2018**, *20*, 679–688. [[CrossRef](#)]
15. Ma, C.; Mu, Z.; Li, J.; Jin, Y.; Cheng, J.; Lu, G.; Hao, Z.; Qiao, S. Mesoporous Co₃O₄ and Au/Co₃O₄ catalysts for low-temperature oxidation of trace ethylene. *J. Am. Chem. Soc.* **2010**, *132*, 2608–2613. [[CrossRef](#)] [[PubMed](#)]
16. Chen, H.; Yang, M.; Tao, S.; Chen, G. Oxygen vacancy enhanced catalytic activity of reduced Co₃O₄ towards p-nitrophenol reduction. *Appl. Catal. B-Environ.* **2017**, *209*, 648–656. [[CrossRef](#)]
17. Chen, H.; Yang, M.; Tao, S.; Ren, M.; Chen, G. Facile Synthesis of Co₃O₄ with different morphologies via oxidation kinetic control and its application in hydrogen peroxide decomposition. *Cryst. Growth Des.* **2016**, *16*, 6286–6293. [[CrossRef](#)]
18. Yan, Q.; Li, X.; Zhao, Q.; Chen, G. Shape-controlled fabrication of the porous Co₃O₄ nanoflower clusters for efficient catalytic oxidation of gaseous toluene. *J. Hazard. Mater.* **2012**, *209–210*, 385–391. [[CrossRef](#)]
19. Xie, X.; Yong, L.; Liu, Z.Q.; Haruta, M.; Shen, W. Low-temperature oxidation of CO catalysed by Co₃O₄ nanorods. *Nature* **2009**, *458*, 746–749. [[CrossRef](#)]
20. Li, R.; Shi, X.; Huang, Y.; Chen, M.; Zhu, D.; Ho, W.; Cao, J.; Lee, S. Catalytic oxidation of formaldehyde on ultrathin Co₃O₄ nanosheets at room temperature effect of enhanced active sites exposure on reaction path. *Appl. Catal. B-Environ.* **2022**, *319*, 121902. [[CrossRef](#)]
21. Mejia, Y.R.; Reddy Bogireddy, N.K. Reduction of 4-nitrophenol using green-fabricated metal nanoparticles. *RSC Adv.* **2022**, *12*, 18661–18675. [[CrossRef](#)] [[PubMed](#)]
22. Wang, S.; Li, Y.; Song, J.; Zhang, J.; Ma, Y. Recent progress in the electrochemical quantification of nitrophenols. *J. Electroanal. Chem.* **2023**, *938*, 117375. [[CrossRef](#)]
23. Zhao, Y.; Yuan, P.; Xu, X.; Yang, J. Removal of p-nitrophenol by adsorption with 2-phenylimidazole-modified ZIF-8. *Molecules* **2023**, *28*, 4195. [[CrossRef](#)]
24. Arora, P.K.; Srivastava, A.; Singh, V.P. Bacterial degradation of nitrophenols and their derivatives. *J. Hazard. Mater.* **2014**, *266*, 42–59. [[CrossRef](#)]
25. Balakrishnan, A.; Gaware, G.J.; Chinthala, M. Heterojunction photocatalysts for the removal of nitrophenol: A systematic review. *Chemosphere* **2023**, *310*, 136853. [[CrossRef](#)] [[PubMed](#)]
26. Khan, S.B.; Akhtar, K.; Bakhsh, E.M.; Asiri, A.M. Electrochemical detection and catalytic removal of 4-nitrophenol using CeO₂-Cu₂O and CeO₂-Cu₂O/CH nanocomposites. *Appl. Surf. Sci.* **2019**, *492*, 726–735. [[CrossRef](#)]
27. Galyaltdinov, S.; Svalova, A.; Brusko, V.; Kirsanova, M.; Dimiev, A.M. Nickel on oxidatively modified carbon as a promising cost-efficient catalyst for reduction of p-nitrophenol. *Molecules* **2022**, *27*, 5637. [[CrossRef](#)]
28. Feng, J.; Su, L.; Ma, Y.; Ren, C.; Guo, Q.; Chen, X.; Feng, J.; Su, L.; Ma, Y.; Ren, C. CuFe₂O₄ magnetic nanoparticles: A simple and efficient catalyst for the reduction of nitrophenol. *Chem. Eng. J.* **2013**, *221*, 16–24. [[CrossRef](#)]
29. Zhao, P.; Feng, X.; Huang, D.; Yang, G.; Astruc, D. Basic concepts and recent advances in nitrophenol reduction by gold- and other transition metal nanoparticles. *Coord. Chem. Rev.* **2015**, *287*, 114–136. [[CrossRef](#)]
30. Elfiad, A.; Galli, F.; Djadoun, A.; Sennour, M.; Chegrouche, S.; Meddour-Boukhobza, L.; Boffito, D.C. Natural alpha-Fe₂O₃ as an efficient catalyst for the p-nitrophenol reduction. *Mater. Sci. Eng. B Solid State Mater. Adv. Technol.* **2018**, *229*, 126–134. [[CrossRef](#)]
31. Pan, L.; Li, L.; Chen, Y. Synthesis of NiO nanomaterials with various morphologies and their electrocatalytic performances for p-nitrophenol reduction. *J. Sol-Gel Sci. Technol.* **2012**, *62*, 364–369. [[CrossRef](#)]
32. Konar, S.; Kalita, H.; Puvvada, N.; Tantubay, S.; Pathak, A. Shape-dependent catalytic activity of CuO nanostructures. *J. Catal.* **2016**, *336*, 11–22. [[CrossRef](#)]

33. Che, W.; Ni, Y.; Zhang, Y.; Ma, Y. Morphology-controllable synthesis of CuO nanostructures and their catalytic activity for the reduction of 4-nitrophenol. *J. Phys. Chem. Solids* **2015**, *77*, 1–7. [[CrossRef](#)]
34. Chiu, H.Y.; Wi-Afedzi, T.; Liu, Y.T.; Ghanbari, F.; Lin, K.Y.A. Cobalt oxides with various 3D nanostructured morphologies for catalytic reduction of 4-nitrophenol: A comparative study. *J. Water Process Eng.* **2020**, *37*, 101379. [[CrossRef](#)]
35. Mogudi, B.M.; Ncube, P.; Meijboom, R. Catalytic activity of mesoporous cobalt oxides with controlled porosity and crystallite sizes: Evaluation using the reduction of 4-nitrophenol. *Appl. Catal. B-Environ.* **2016**, *198*, 74–82. [[CrossRef](#)]
36. Chen, Z.; Wang, S.; Liu, W.; Gao, X.; Gao, D.; Wang, M.; Wang, S. Morphology-dependent performance of Co₃O₄ via facile and controllable synthesis for methane combustion. *Appl. Catal. A-Gen.* **2016**, *525*, 94–102. [[CrossRef](#)]
37. Pacchioni, S.; Antonio Ruiz, P.; Gianfranco, P. Role of metal/oxide interfaces in enhancing the local oxide reducibility. *Top. Catal.* **2019**, *62*, 1192–1201.
38. Mogudi, B.M.; Ncube, P.; Bingwa, N.; Mawila, N.; Mathebula, S.; Meijboom, R. Promotion effects of alkali- and alkaline earth metals on catalytic activity of mesoporous Co₃O₄ for 4-nitrophenol reduction. *Appl. Catal. B-Environ.* **2017**, *218*, 240–248. [[CrossRef](#)]
39. Rabee, A.I.M.; Gaid, C.B.A.; Mekhemer, G.A.H.; Zaki, M.I. Combined TPR, XRD, and FTIR studies on the reduction behavior of Co₃O₄. *Mater. Chem. Phys.* **2022**, *289*, 126367. [[CrossRef](#)]
40. Sun, J.; Fu, Y.; He, G.; Sun, X.; Wang, X. Catalytic hydrogenation of nitrophenols and nitrotoluenes over a palladium/graphene nanocomposite. *Catal. Sci. Technol.* **2014**, *4*, 1742–1748. [[CrossRef](#)]
41. Jiang, Y.; Li, W.; Chen, K.; Zhang, X.; Shen, C.; Yuan, L. A rod-like Co₃O₄ with high efficiency and large specific surface area for lean methane catalytic oxidation. *Mol. Catal.* **2022**, *522*, 112229. [[CrossRef](#)]
42. Hu, L.; Liu, X.; Guo, A. Cobalt with porous carbon architecture: Towards of 4-nitrophenol degradation and reduction. *Sep. Purif. Technol.* **2022**, *288*, 120595. [[CrossRef](#)]
43. Triveni, R.M.; Buvaneswari, G. Catalytic activity of first row transition metal oxides in the conversion of p-nitrophenol to p-aminophenol. *J. Mol. Catal. A-Chem.* **2011**, *350*, 9–15.
44. Hu, W.; Shao, Z.J.; Cao, X.M.; Hu, P. Multi sites vs. single site for catalytic combustion of methane over Co₃O₄: A first-principles kinetic Monte Carlo study. *Chin. J. Catal.* **2020**, *41*, 1369–1377. [[CrossRef](#)]
45. Din, M.I.; Khalid, R.; Hussain, Z.; Hussain, T.; Mujahid, A.; Najeeb, J.; Izhar, F. Nanocatalytic assemblies for catalytic reduction of nitrophenols: A critical review. *Crit. Rev. Anal. Chem.* **2020**, *50*, 322–338. [[CrossRef](#)] [[PubMed](#)]
46. Huang, L.; Zhang, H.; He, Z.; Chen, J.; Song, S. In situ formation of nitrogen-doped carbon-wrapped Co₃O₄ enabling highly efficient and stable catalytic reduction of p-nitrophenol. *Chem. Commun.* **2020**, *56*, 770–773. [[CrossRef](#)]
47. Burda, C.; Chen, X.; Narayanan, R.; El-Sayed, M.A. Chemistry and properties of nanocrystals of different shapes. *Chem. Rev.* **2005**, *105*, 1025–1102. [[CrossRef](#)]
48. Daniel, M.C.; Astruc, D. Gold nanoparticles: Assembly, supramolecular chemistry, quantum-size-related properties, and applications toward biology, catalysis, and nanotechnology. *Chem. Rev.* **2004**, *104*, 293–346. [[CrossRef](#)]
49. Wu, J.; Liu, W.; Xiang, X.; Sun, K.; Liu, F.; Cai, C.; Han, S.; Xie, Y.; Li, S.; Zu, X. From Ni(OH)₂/Graphene composite to Ni@Graphene core-shell: A self-catalyzed epitaxial growth and enhanced activity for nitrophenol reduction. *Carbon* **2017**, *117*, 192–200. [[CrossRef](#)]
50. Roy, M.; Ghosh, S.; Naskar, M.K. Synthesis of morphology controllable porous Co₃O₄ nanostructures with tunable textural properties and their catalytic application. *Dalton Trans.* **2014**, *43*, 10248–10257. [[CrossRef](#)]
51. Oueslati, M.H.; Ben Tahar, L.; Harrath, A.H. Synthesis of ultra-small gold nanoparticles by polyphenol extracted from *Salvia officinalis* and efficiency for catalytic reduction of p-nitrophenol and methylene blue. *Green Chem. Lett. Rev.* **2020**, *13*, 18–26. [[CrossRef](#)]
52. Swain, S.; Bhavya, M.B.; Kandathil, V.; Bhol, P.; Patil, S.A. Controlled synthesis of palladium nanocubes as an efficient nanocatalyst for Suzuki-Miyaura cross-coupling and reduction of p-nitrophenol. *Langmuir* **2020**, *36*, 5208–5218. [[CrossRef](#)] [[PubMed](#)]
53. Harika, V.K.; Sadhanala, H.K.; Perelshtein, I.; Gedanken, A. Sonication-assisted synthesis of bimetallic Hg/Pd alloy nanoparticles for catalytic reduction of nitrophenol and its derivatives. *Ultrason. Sonochem.* **2019**, *60*, 104804. [[CrossRef](#)] [[PubMed](#)]
54. Liu, D.; Wang, Z.; Ma, Y.; Xu, C.; Zhou, S. Au-Cu_xO_y nanoparticles encapsulated in hollow porous silica nanospheres as efficient catalysts for nitrophenol reduction. *ACS Appl. Nano Mater.* **2022**, *6*, 461–468. [[CrossRef](#)]
55. Shanmugaraj, K.; Bustamante, T.M.; Torres, C.C.; Campos, C.H. Gold nanoparticles supported on mesostructured oxides for the enhanced catalytic reduction of 4-nitrophenol in water. *Catal. Today* **2020**, *388–389*, 383–393. [[CrossRef](#)]
56. Zhou, X.; Bai, X. PdCu alloy prepared by ultrasonic method catalyzes the degradation of p-nitrophenol. *Environ. Sci. Pollut. Res.* **2023**, *30*, 48449–48459. [[CrossRef](#)]
57. Chernykh, M.; Mikheeva, N.; Zaikovskii, V.; Salaev, M.; Mamontov, G. Room-temperature nitrophenol reduction over Ag-CeO₂ catalysts: The role of catalyst preparation method. *Catalysts* **2020**, *10*, 580. [[CrossRef](#)]
58. Zhang, S.; Zhong, L.; Xu, Z.; Hu, J.; Tang, A.; Zuo, X. Mineral-modulated Co catalyst with enhanced adsorption and dissociation of BH₄⁻ for hydrogenation of p-nitrophenol to p-aminophenol. *Chemosphere* **2022**, *291*, 132871. [[CrossRef](#)]
59. Dou, S.; Zhou, S.; Huang, H.; Yan, P.; Shoko, E.; Isimjan, T.T.; Yang, X. Metal-organic framework (MOF)-derived electron-transfer enhanced homogeneous PdO-rich Co₃O₄ as a highly efficient bifunctional catalyst for sodium borohydride hydrolysis and 4-nitrophenol reduction. *Chemistry* **2020**, *26*, 16923–16931. [[CrossRef](#)]

60. Zoltowska, S.; Minambres, J.F.; Piasecki, A.; Mertens, F.; Jesionowski, T. Three-dimensional commercial-sponge-derived $\text{Co}_3\text{O}_4@C$ catalysts for effective treatments of organic contaminants. *J. Environ. Chem. Eng.* **2021**, *9*, 105631. [[CrossRef](#)]
61. Hunge, Y.M.; Yadav, A.A.; Kang, S.W.; Kim, H.; Fujishima, A.; Terashima, C. Nanoflakes-like nickel cobaltite as active electrode material for 4-nitrophenol reduction and supercapacitor applications. *J. Hazard. Mater.* **2021**, *419*, 126453. [[CrossRef](#)] [[PubMed](#)]

Disclaimer/Publisher's Note: The statements, opinions and data contained in all publications are solely those of the individual author(s) and contributor(s) and not of MDPI and/or the editor(s). MDPI and/or the editor(s) disclaim responsibility for any injury to people or property resulting from any ideas, methods, instructions or products referred to in the content.